


Deep-learning interatomic potential for iron at extreme conditionsZhi Li * and Sandro Scandolo †*The Abdus Salam International Centre of Theoretical Physics, Strada Costiera 11, 34151 Trieste, Italy* (Received 22 November 2023; revised 25 March 2024; accepted 2 May 2024; published 14 May 2024)

Atomistic simulations play an important role in elucidating the physical properties of iron at extreme pressure and temperature conditions, which in turn provide crucial insights into the present state and thermal evolution of the earth's and planetary cores. However, simulations face challenges in retaining *ab initio* accuracy at the simulation size and time scales required to address some of the most important geophysical questions. We used deep-learning methods to develop interatomic models for iron covering pressures from 75–650 GPa and temperatures from 4000–7600 K. The models retain *ab initio* accuracy while being computationally cost effective. Rigorous validation tests attest their accuracy in large-scale simulations as well as in the presence of extended defects. The models pave the way to the determination of the thermodynamic and rheological properties of iron at extreme conditions with *ab initio* accuracy.

DOI: [10.1103/PhysRevB.109.184108](https://doi.org/10.1103/PhysRevB.109.184108)**I. INTRODUCTION**

The physical properties of iron, the main constituent of planetary cores, have attracted significant attention over the past two decades [1]. Extensive theoretical [2–7] and experimental studies [8–10] have addressed its phase diagram and physical properties at the relevant pressure and temperature conditions, which in the case of the earth's core are in the range of 130–360 GPa and 4000–7000 K. Determining these properties is crucial to model the structure and the thermal evolution of the core. For example, the melting temperature of iron serves as a reference for estimates of the earth's core thermal gradient [11], while the crystal structure, viscosity, and rheology of Fe at earth's inner core conditions hold crucial information for the interpretation of seismic observations [12–16].

Experimental determination of these properties in the laboratory is hindered by difficulties in reaching the relevant pressure and temperature conditions in a controlled fashion. Atomistic simulations play an essential role in this context (e.g., Refs. [2,17]), but they are challenged by the large sizes and long times required to achieve convergence on the statistical averages and by the necessity to retain the energetic accuracy that is necessary, e.g., to distinguish between the different phases. Atomistic simulations hinge on the specification of a model to describe the interatomic potential, i.e., of the potential energy surface as a function of the atom coordinates. In principle, an accurate description of the interatomic interaction is provided by density-functional theory (DFT) and its high-temperature extension [18–20]. However, the substantial computational demands of DFT restrict its application to systems with just a few hundred atoms, which are inadequate to describe some of the most geophysically relevant properties

of iron. For example, the simulation of body-centered cubic (bcc) iron, a potential candidate for the crystal structure of iron in the inner core, is affected by significant finite-size effects due to the presence of large atomic self-diffusion [12]. Moreover, rheological properties, a crucial ingredient in the understanding of seismic attenuation and anisotropy, have their microscopic basis in the behavior of extended defects such as grain boundaries and dislocations [21], whose simulation requires simulation cells containing several thousand and even up to 10^6 atoms [22]. Parametrized interatomic potentials such as the embedded-atom model (EAM) can reach these system sizes and have been widely employed to study iron at core conditions. However, the accuracy of EAM models in estimating free energies is limited [23], especially considering that Gibbs free energy differences among various iron polymorphs are estimated by DFT to be in the range of a few tens of meV per atom [4,5,24].

Deep-learning potentials (DP) based on a deep neural network (DNN) have recently emerged as an efficient method to address these limitations [25–27], thanks to their ability to accurately describe the DFT potential energy surface in a computationally cost-effective manner. In this study, we employ the deep-potential method to construct and validate a set of potentials for iron that describe the various phases, including the hexagonal close-packed (hcp) structure, the bcc structure, the face-centred cubic (fcc) structure, and the liquid phase with an accuracy comparable to that of DFT in the temperature range 4000–7600 K and in the pressure range 75–650 GPa, with a special focus on the pressure-temperature conditions near the melting curve, which are most relevant for geophysics. The remainder of this paper is organized as follows. First, we describe the construction process of the DP models. Then, we present an extensive validation of the models, covering a wide range of physical properties. We also compare the performance of our models with that of the EAM potential developed in Ref. [17]. We stress that the purpose of this work is to validate the DP models as an accurate proxy

*zli@ictp.it

†scandolo@ictp.it

of the DFT potential energy surface, and not to compare DP models (nor DFT) to experimental observations.

II. METHODOLOGY

A. Density-functional theory calculations

A fundamental ingredient in the construction of an interatomic DP model is the definition of the reference system that the model is expected to reproduce. While higher levels of theory than DFT have been considered in the study of Fe at high pressure, such as quantum Monte Carlo [28] and dynamical mean-field theory [29], none of them are able to include the effects of temperature on the electronic degrees of freedom. On the other hand, DFT has shown an excellent performance in reproducing experimental data at extreme conditions, as long as proper attention is paid to the relevant approximations [30,31]. In this work, energy, forces, and stress tensor are obtained within the framework of finite-temperature density functional theory, where the thermal excitation of the electrons is explicitly included through the Mermin functional in a Kohn-Sham framework [18–20].

Calculations were performed using the QUANTUM ESPRESSO code [32,33]. For the iron pseudopotential, we employed the projected augmented wave method [34], treating the $3s^23p^64s^23d^6$ electrons as valence electrons. The exchange-correlation term was based on the generalized gradient approximation proposed by Perdew-Burke-Ernzerhof (PBE) [35]. We set the kinetic energy cutoff for the plane-wave basis to 200 Ry. Kohn-Sham band occupancies were determined using the Fermi-Dirac distribution, with a width corresponding to the simulation temperature. Unless otherwise stated, we sampled the Brillouin zone with a $2 \times 2 \times 2$ k -points mesh [36] for systems containing fewer than 300 atoms, while systems larger than that were sampled using only the Γ point. This sampling scheme ensures a pressure and energy accuracy of 0.5 meV/atom and 0.5 kbar, respectively. We do not consider the effect of magnetism, as previous work [4] and our own tests indicate that thermal electronic excitations lead to a vanishing magnetic moment at high temperatures.

For the calculation of generalized stacking-fault (GSF) energies we employed simulation cells with varying numbers of atoms, depending on the specific slip system under investigation. We fixed the length along the z direction (orthogonal to the slip plane) at approximately twice the size of the other dimensions. When examining the $1/2\langle 110 \rangle\{111\}$ slip system in fcc iron, we used a simulation cell consisting of 144 atoms. In the case of hcp iron, we investigated five slip systems, including basal, prismatic, pyramidal $\langle c+a \rangle$ first-order, pyramidal $\langle a \rangle$, and pyramidal $\langle c+a \rangle$ second-order slip systems. For the first four slip systems, we employed a 144-atom simulation cell, whereas for the pyramidal $\langle c+a \rangle$ second-order slip system we utilized a 128-atom simulation cell. Simulation cells were generated using the ATOMSK code [37], and for all GSF calculations we used a k -points mesh of $2 \times 2 \times 1$ to sample the Brillouin zone.

B. Deep-potential model and its construction

In finite-temperature DFT calculations the potential energy surface, i.e., the energy of the system as a function of the

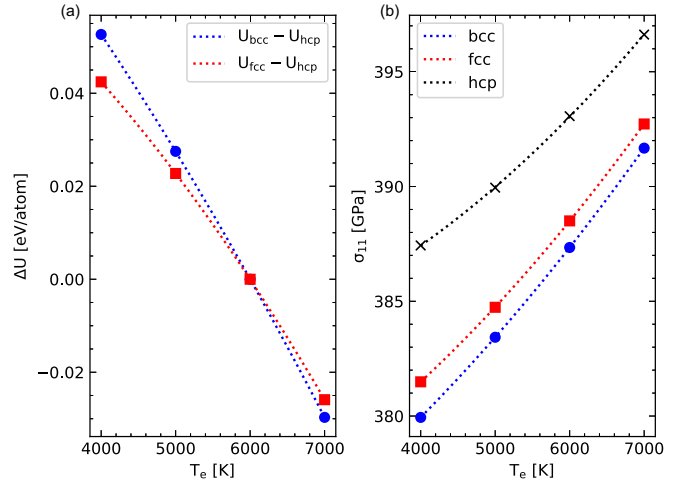


FIG. 1. (a) DFT energy differences and (b) a selected component (σ_{11}) of the DFT stress tensor calculated with different electronic temperatures on the same bcc, fcc, and hcp configurations. The configurations were generated with the DP model at 6000 K. DFT energy differences are expressed relative to the energy differences calculated at an electronic temperature of 6000 K. The dotted line is a second-order polynomial fit and serves as a guide to the eye.

atomic positions, has an explicit temperature dependence that stems from the different Fermi-Dirac occupation of the electronic orbitals at different temperatures. As a consequence, different DP models must be constructed for simulations at different temperatures. For an intuitive understanding of the effects of electronic temperature on the interatomic potential, we extracted a single snapshot for each phase (bcc, fcc, and hcp iron) from molecular dynamics simulations at 6000 K. The configurations included 250, 256, and 216 atoms, for bcc, fcc, and hcp, respectively. We calculated the *ab initio* potential energy and the virial stress tensor on those configurations by just varying the electronic temperature from 4000–7000 K. As shown in Fig. 1, DFT potential energy differences change by as much as 80 meV/atom for bcc iron and 60 meV/atom for fcc iron, with respect to hcp iron, by changing the electronic temperature. Within the considered temperature range, the diagonal component of the stress along the x direction changes by approximately 10 GPa. As we will see later, these changes are much larger than the accuracy reached by a DP model in simulations conducted at the same temperature at which the model is constructed.

While some approximate solutions have been proposed to incorporate the temperature dependence in the interatomic potential [38,39], it is clear that in order for the DP models to retain the highest accuracy, different models must be generated at different temperatures. In the following we show how a set of DP models generated at 4000, 5000, 6000, 7000, and 7600 K is sufficient to retain the highest accuracy in reproducing DFT energy surfaces at all temperatures within the same temperature range.

As a first step we developed a DP model at 6000 K. We will show that DP models at different temperatures can be generated with minimal effort by refinement of the DP model at 6000 K.

DP models are generated using the DeePMD-kit [40]. DeePMD-kit employs two neural networks, including embedding and fitting nets, to predict the total energy. The initial atomic coordinates are first passed as input to the embedding neural network to determine the relative displacements of all neighboring atoms within a cutoff radius of 8 Å around a central atom. The sizes of the hidden layers in the embedding net are (25, 50, 100), and the first 16 columns of the output matrix are selected to form another submatrix. Matrix multiplication is then performed using the output matrix and the submatrix to construct the structural descriptor. To ensure a continuous change in the descriptor, a switching function, varying from 1 at a distance of 2 Å to 0 at 8 Å, is used to weigh the relative displacements. If the distance is less than 2 Å, the weight is automatically set to 1. The resulting structural descriptor is then passed to the fitting net to obtain the total energy, the sizes of which in its hidden layers are (240, 240, 240). Force and stress tensors can be computed accordingly, based on the analytical derivation of energy with respect to position and strain. The loss function is constructed as a weighted sum of the root-mean-square errors (RMSE) of energy (E_ϵ), pressure (σ_ϵ), and force (F_ϵ), which are defined as,

$$E_\epsilon = \frac{\sqrt{\sum_{i=1}^{N_s} (E_{\text{DP}}^i - E_{\text{DFT}}^i)^2}}{N_s} \quad (1)$$

$$\sigma_\epsilon = \frac{\sqrt{\sum_{i=1}^{N_s} \sum_{\alpha=1}^3 \sum_{\beta=\alpha}^3 (\sigma_{\text{DP}}^{\alpha\beta} - \sigma_{\text{DFT}}^{\alpha\beta})^2}}{6N_s} \quad (2)$$

$$F_\epsilon = \frac{\sqrt{\sum_{i=1}^{N_s} \sum_{j=1}^{N_a} \sum_{\alpha=1}^3 (F_{\text{DP}}^{i j \alpha} - F_{\text{DFT}}^{i j \alpha})^2}}{3N_a N_s}, \quad (3)$$

where N_s represents the total number of structures in the data set, N_a is the number of atoms in one structure, the subscript DP indicates the quantities predicted by the DP model, while the subscript DFT denotes quantities calculated by DFT. During the training process, the learning rate exponentially decays, with starting and final learning rates set to 1×10^{-3} and 3×10^{-8} , respectively, with a decay step of 2000. For each active-learning cycle, the DP models are trained with 4×10^5 steps with the initial values for the neural network parameters set to the values learned in the last cycle. The weights for energy, force, and stress tensor in the loss function are gradually adjusted based on the learning rate. The starting weights are set to 0.02, 1000, and 0.02, respectively, while the final weights are all set to 1. After the active-learning process converges, the DP models are further trained with 1×10^6 steps. More technical details regarding the construction of the structural descriptor, the fitting net, and the training algorithm can be found in Zhang *et al.* [41].

We employ an iterative or active-learning scheme to generate the training data set for developing the DP model at 6000 K [2]. The process is initiated with a few seed structures obtained by distorting the perfect hcp, bcc, and fcc structures, each containing 144, 128, and 108 atoms, respectively. Additionally, we include a few liquid iron structures, consisting of 108 atoms, extracted from our previous work [42]. We then train four potentials using the same neural network hyperparameters (see above) but with different random seeds. Subsequently, we conduct classical molecular dynamics (MD)

simulations using LAMMPS [43] in the NPT ensemble with the four DP models at 6000 K and pressures ranging from 250–400 GPa, with an interval of 25 GPa. The Nosé-Hoover thermostat and barostat [44,45] are employed to control temperature and pressure. We randomly pick approximately 100 structures from the obtained MD trajectories and calculate the RMSE between the four potentials of each structure. Structures with a large RMSE on the forces (0.2 eV/Å to 0.35 eV/Å) are added to the training data set and fed to first-principles calculations to obtain forces, energies, and pressures. This entire process is iterated until the fraction of selected configurations falls below 10%. The same procedure is followed to generate structures for hcp, bcc, fcc, and liquid iron, each containing 216, 250, 256, and 200 atoms, respectively. This step is essential to make the DP model applicable to larger systems by capturing possible long-range interactions.

Finally, the DP model trained at 6000 K was employed as the basis for further refinement at other temperatures, following the same procedure. The composition of the training data sets, along with the performance of the DP models on their respective training datasets are shown in Table I. For all conditions, the RMSE of energy, pressure, and force is below 5.0 meV/atom, 0.56 GPa, and 0.30 eV/Å, respectively. We found no distinctions in the performance of models at different temperatures. However, almost one order of magnitude more structures were used to train the DP model at 6000 K than at the other temperatures, confirming that the refinement process is much faster than fitting a potential from scratch.

III. VALIDATION OF THE DEEP POTENTIAL MODELS

A. Performance on the testing data set

In order to validate the DP models we first create an independent testing data set to assess whether the performance remains consistent for structures not included in the training data set. The testing data set encompasses hcp, fcc, bcc, and liquid iron structures in a wide range of thermodynamic conditions. The data set is generated by conducting molecular dynamics simulations using the obtained DP models, from which we extract 15 configurations at each condition, spaced evenly at 1 ps intervals. The relatively long interval between configurations is intended to reduce the correlation between consecutive snapshots. In order to evaluate the performance of the developed DP models across different system sizes we considered, for each phase, structures containing different numbers of atoms. For example, the testing data set for hcp iron includes structures with 144 and 216 atoms, respectively. As shown in Fig. 2, at all pressure-temperature conditions, the maximum RMSE for energy, pressure, and force is 5.0 meV/atom, 0.65 GPa, and 0.30 eV/Å for solid phases, and 6.4 meV/atom, 0.8 GPa, and 0.35 eV/Å for the liquid phase. We do not observe a substantial change in the performance of the DP models across different phases and pressure-temperature conditions. Furthermore, the consistent performance on the test data compared to that on the training data suggests that our DP model is not affected by over- or underfitting problems. Considering that the models are generated at different temperatures and thus different amounts of

TABLE I. The root-mean-square error of energy (E_ϵ), force (F_ϵ), and pressure (P_ϵ) for the training data set, along with the number of structures for each phase (shown in two columns below each phase), containing two different sizes with the smaller size on the left and the larger one on the right. For hcp iron, we employ 144 and 216 atoms, while for bcc iron, 128 and 250 atoms are used. The calculations for fcc iron were performed with 108 and 256 atoms, respectively, while for the liquid phase, we employ 108- and 200-atom cells.

T (K)	E_ϵ (meV/atom)	P_ϵ (GPa)	F_ϵ (eV/Å)	hcp		fcc		bcc		Liquid	
4000 ^a	3.3	0.43	0.25	578	139	750	139	799	139	280	50
5000 ^b	3.5	0.45	0.26	464	109	605	110	640	110	340	60
6000 ^c	3.4	0.47	0.26	1139	1169	917	1154	1222	947	600	280
7000 ^d	3.7	0.50	0.27	209	50	275	50	300	50	300	50
7600 ^e	3.3	0.56	0.30	137	31	128	32	165	91	185	150

^aAt 4000 K, hcp, fcc, and bcc iron were trained in 75–400 GPa, while liquid iron was trained in 75–175 GPa.

^bAt 5000 K, hcp, fcc, and bcc iron were trained in 175–400 GPa, while liquid iron was trained in 125–250 GPa.

^cAt 6000 K, all phases were trained in 250–400 GPa.

^dAt 7000 K, all phases were trained in 350–450 GPa.

^eAt 7600 K, all phases were trained in 450–650 GPa.

thermal fluctuations, it is useful to assess the performance of DP models in a relative sense by normalizing the difference in force between DFT and DP by the average magnitude of the forces from DFT simulations,

$$\Delta F_\epsilon = \frac{\sqrt{\sum_{i=1}^{N_s} \sum_{j=1}^{N_a} \sum_{\alpha=1}^3 (F_{DP}^{ij\alpha} - F_{DFT}^{ij\alpha})^2}}{\sqrt{\sum_{i=1}^{N_s} \sum_{j=1}^{N_a} \sum_{\alpha=1}^3 (F_{DFT}^{ij\alpha})^2}}. \quad (4)$$

We found that the relative force error for all phases at all thermodynamic conditions is below 10%.

As a further illustration of the ability of the DP models to reproduce the DFT we conducted an MD simulation for hcp iron with 96 atoms and $c/a = 1.612$ and 1.615 in the canonical ensemble at 6000 K, with the DP model. From these simulations we extracted 25 snapshots evenly spaced over a 1 ps intervals and calculated DFT values of energy, forces, and

stress. As demonstrated in Fig. 3, the DP model demonstrates a remarkable ability to accurately match the DFT simulation results even for $\Delta\sigma = \sigma_{11} - \sigma_{33}$, a quantity that is important for determining the equilibrium c/a for the hcp structure.

B. Performance on large systems

We have shown that the performance of the DP models is independent of the number of atoms for all iron phases. To further confirm the absence of finite-size effects, we compare in Fig. 4 the RMSEs for systems with more than 400 atoms. Due to the significant computational cost, we only conducted analyses at a few selected pressure-temperature conditions with ten structures. The maximum RMSE error for energy, force, and pressure is 5 meV/atom, 0.35 eV/Å, and 0.6 GPa, respectively. Despite its limited statistical significance, the test

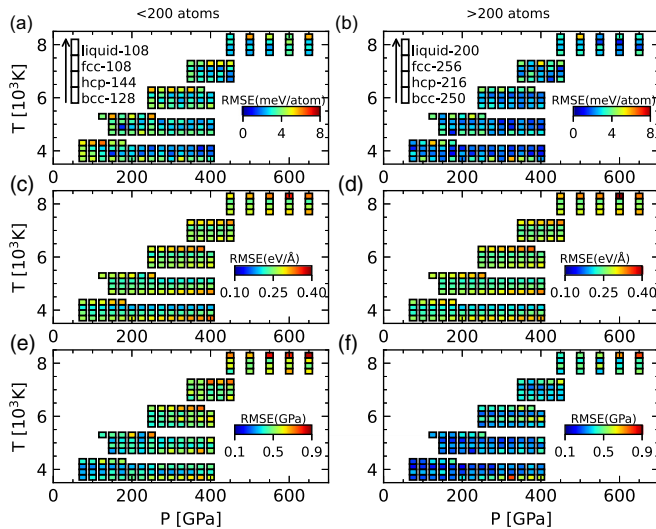


FIG. 2. Performance of the DP models on the test data set. The test data set includes hcp, fcc, bcc, and liquid iron configurations. In total, five DP models were trained, at 4000, 5000, 6000, 7000, and 7600 K, respectively. The root-mean-square error (RMSE) is used to measure the differences between the values predicted by a DP model and the values calculated by DFT.

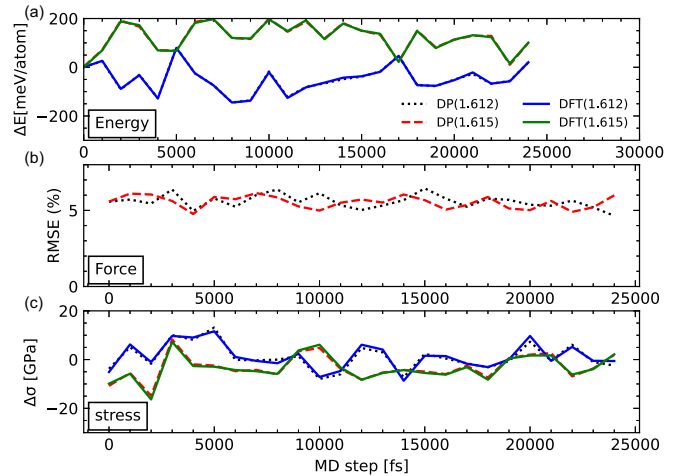


FIG. 3. Comparison of (a) DP model energies, (b) forces, and (c) stress with respect to DFT values, on a molecular dynamics simulation of hcp iron with different values of c/a (1.612 and 1.615). Energies are expressed as ΔE relative to the energy of the first snapshot. Errors on forces are reported as RMSE, as defined in Eq. (4). To illustrate the accuracy on the stress tensor, the value of $\Delta\sigma = \sigma_{33} - \sigma_{11}$ is reported as it is the component that determines the c/a ratio for hcp iron.

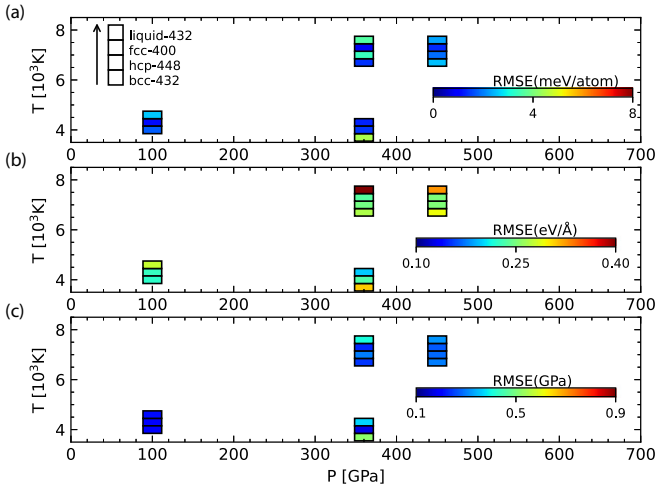


FIG. 4. Performance of the deep potential models for systems with more than 400 atoms. Due to the significant computational cost, RMSE is computed for (a) energy, (b) force, and (c) pressure at select thermodynamic conditions, each with ten configurations at 4000 K and 7000 K, respectively.

indicates that there is no degradation in the performance of the model in large systems. Therefore, we conclude that the developed DP models are well suited for large-scale simulations.

C. Comparison with other classical potentials

Embedded-atom models (EAM) are commonly used for simulating metallic systems like iron. Although their analytical form reflects the relevant microscopic physics of the interatomic forces, the relatively small number of adjustable parameters does not allow us to take full advantage of the massive amount of information that is present in our training data sets. As a consequence, their performance in reproducing DFT data is limited. As an example, we show in Fig. 5 the performance of the EAM potential developed in Ref. [17] in reproducing DFT data for some of the configurations present in our training data set. The EAM potential yields an error in the forces of at least 20% in the solid phases and its performance degrades at the highest temperatures, particularly for the liquid phase, with an error on the forces as high as 50%. For comparison the relative RMSE of forces for the DP model on the same configurations remains below 6% and shows little change with temperature. We believe that evaluating the accuracy of a model at the microscopic level (e.g., on individual forces) is an important test to evaluate the predictivity of the model on physical quantities other than the ones present in the loss function (energy and stress tensor).

D. Accuracy in the Gibbs free energy

One of the objectives of atomistic simulations is the determination of phase diagrams. In the specific case of iron, the focus is on the evaluation of the relative thermodynamic stability of the hcp, fcc, and bcc structures. To this aim it is essential to understand the accuracy of the Gibbs free energy obtained from DP models compared to their DFT counterpart. The Gibbs free-energy difference between the DP model and

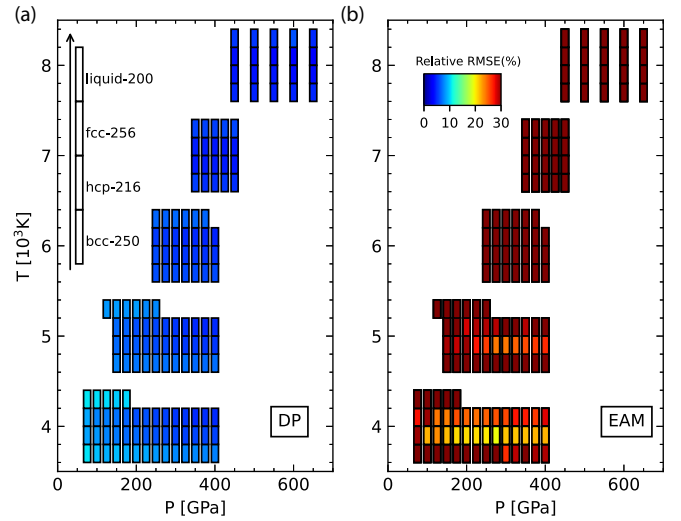


FIG. 5. Performance comparison between (a) DP models and (b) the EAM potential with respect to force. For simplicity, this comparison only utilizes the testing data set with more than 200 atoms. The relative RMSE error, as defined in Eq. (4), is used to measure the force difference relative to DFT potentials.

DFT can be expressed as,

$$\Delta G = G_{\text{DFT}} - G_{\text{DP}} = -\frac{1}{\beta} \ln(\langle \exp(-\beta(U_{\text{DFT}} - U_{\text{DP}})) \rangle), \quad (5)$$

where the ensemble average $\langle \dots \rangle$ is performed over configurations sampled from the isobaric-isothermal ensemble using the DP model, and U is the potential energy [46,47]. We stress that U_{DFT} includes the electronic free energy at the relevant temperature.

Having determined that DP models accurately describe DFT energies, we can compute the Gibbs free energy difference in (5) using free energy perturbation theory [46,47]. To assess the validity of perturbation theory we follow Ref. [23] and introduce the fluctuation strength (σ) as:

$$\sigma = \sqrt{\frac{\langle (\delta \Delta U)^2 \rangle}{N}}, \quad (6)$$

where $\delta \Delta U = U_{\text{DFT}} - U_{\text{DP}} - \langle U_{\text{DFT}} - U_{\text{DP}} \rangle$ and the ensemble average $\langle \dots \rangle$ is performed over configurations drawn from the isobaric-isothermal ensemble using the DP models. We have tabulated the fluctuation strength at various thermodynamic conditions in Table II. We exclusively considered structures with more than 400 atoms, as these large-size

TABLE II. The fluctuation strength (σ), which characterizes the accuracy of the DP models, is calculated at several thermodynamic conditions. The unit of is σ is meV. The parentheses following each phase represents the number of atoms used in the simulations.

P (GPa)	T (K)	bcc (432)	fcc (400)	hcp (448)	Liquid (432)
100	4000	–	19.2	35.2	53.3
360	4000	31.0	23.1	30.0	–
360	7000	25.4	16.5	43.8	53.2
450	7000	49.3	26.4	36.1	47.4

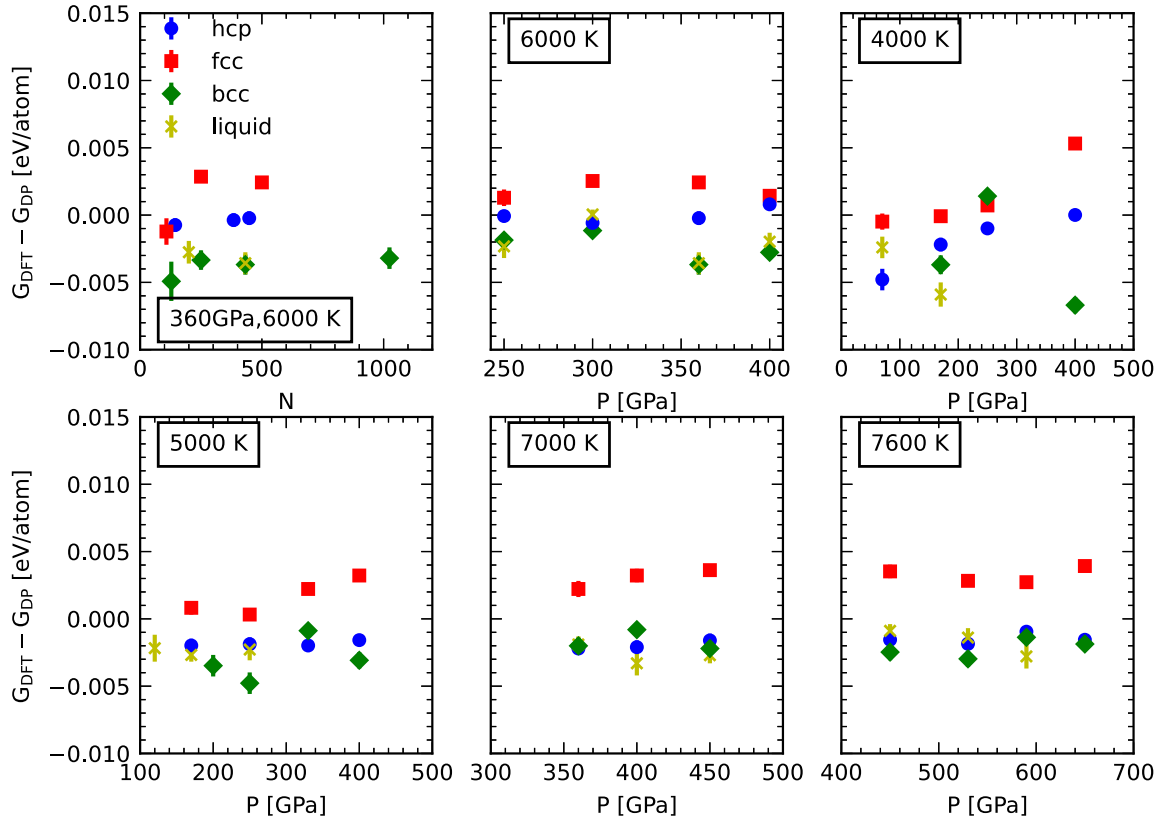


FIG. 6. The Gibbs free energy difference between DP and DFT at 4000, 5000, 6000, 7000, and 7600 K as a function of pressure. The blue circles represent hcp iron, while the green diamonds denote bcc iron. The yellow crosses represent the liquid phase and the red squares denote the fcc phase.

structures are not present in the training data set. The obtained values are significantly smaller than $k_B T$ (345 meV at 4000 K and 603 meV at 7000 K), which justifies the application of perturbation theory. In this case, we can expand Eq. (5) further and retain only up to the second-order terms [23],

$$\Delta G = \langle U_{\text{DFT}} - U_{\text{DP}} \rangle - \frac{\beta}{2} \langle (\delta \Delta U)^2 \rangle. \quad (7)$$

in Fig. 6 we show the calculated Gibbs free energy difference between the DP model and DFT at different pressures and temperatures, for the different phases considered in this work. The calculations were performed with simulation cells containing 432, 500, 432, and 448 atoms for bcc, fcc, liquid, and hcp iron, respectively. The Gibbs free energy difference between the DP models and DFT is generally less than 6 meV/atom and is independent of the system size. To provide context for these values, if we assume that the change in entropy during melting is of the order of $k_B T$, then the above values imply a shift of the melting temperature between the DP model and DFT of approximately 70 K. It is important to remark that Eq. (7) provides a rigorous method to correct Gibbs free energies calculated with the DP model and obtain the corresponding DFT values, bypassing the need for a full *ab initio* sampling of the phase space.

Throughout this paper the DP models generated at a given temperature are used exclusively for simulations at the same temperature at which they have been generated. However, we

believe it is of interest to examine the performance of DP models at different temperatures with respect to the one where they have been generated. To this aim we tested the performance of DP models generated at 4000, 5000, and 7000 K, in reproducing free energy differences between crystal structures at 6000 K and 400 GPa. As shown in Fig. 7, not surprisingly the DP model performing best at 6000 K is the one generated

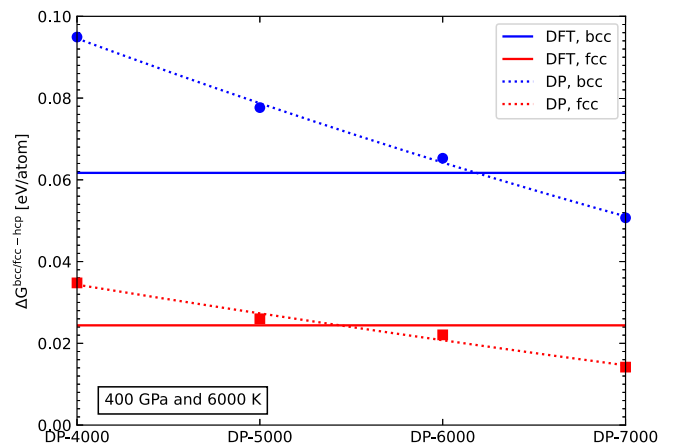


FIG. 7. Gibbs free energy differences between solid phases at 6000 K and 400 GPa, calculated with DP models generated at 4000 K (DP-4000), 5000 K (DP-5000), 6000 K (DP-6000), and 7600 K (DP-7600). DFT values are also shown for comparison.

at 6000 K. However, we find that the DP model generated at 5000 K gives for the bcc-hcp free energy difference at 6000 K, a value which differs by only 17 meV/atom with respect to the value obtained with the DP model generated at 6000 K. The difference is smaller than the bcc-hcp free energy difference and suggests a range of applicability of the DP models of at least ± 1000 K around the temperature at which they have been generated. The DP model generated at 5000 K was fitted to the DFT energy calculated with the electrons at 5000 K. In Fig. 1 we showed that the DFT energy difference between a bcc configuration and an hcp configuration increases by an amount as large as 28 meV by simply changing the electronic temperature in the DFT calculation from 6000 K to 5000 K. The behavior of our DP models is consistent with the fact that they have been obtained from DFT calculations performed at different electronic temperatures, however the dependence on temperature of the DP models (Fig. 7) appears to be milder with respect to the DFT calculations (Fig. 1).

E. Phonon spectrum for bcc iron at 5000 K with self-consistent harmonic approximation

Phonon dispersions not only provide invaluable insights into the intrinsic phonon transport mechanism, but also stand as a benchmark to validate the accuracy of forces in the developed DP models. The test is especially stringent in the case of bcc iron, which is known to achieve dynamical stability only when anharmonic effects are incorporated. Luo *et al.* [13] employed the self-consistent *ab initio* lattice dynamics method to study the dynamical stability of bcc iron with 64 atoms at high temperatures. They discovered that at $7.35 \text{ \AA}^3/\text{atom}$ and 5000 K, which corresponds to a static pressure of 235 GPa and approximately 260 GPa when the kinetic energy contribution is considered, bcc iron is vibrationally stable without showing any imaginary mode. To further validate the accuracy of the forces in our developed DP models, we revisited the vibrational stability of bcc iron using the stochastic self-consistent harmonic approximation (SSCHA) [48], a rigorous variational method that directly yields the anharmonic free energy. The necessary inputs for SSCHA calculations, including force, energy, and stress, were obtained from our constructed DP models. We used a population of 1024 configurations to minimize the statistical noise in SSCHA. The auxiliary phonon frequencies for bcc iron, derived from the simulation at $7.35 \text{ \AA}^3/\text{atom}$ and 5000 K, are reported in Fig. 8. A remarkable alignment is observed when compared with Luo *et al.* [13]. Additionally, we found that the finite-size effects are minimal, and a bcc iron configuration with 64 atoms ($4 \times 4 \times 4$) is adequate to achieve a converged auxiliary phonon spectrum.

F. Radial distribution function

The radial distribution function (RDF) is a valuable tool for characterizing the local atomic structure of solids and liquids. We computed the RDFs for bcc, fcc, hcp, and liquid iron using the DP models and compared them with results obtained from both DFT and classical (EAM) molecular dynamics simulations [42,49]. Figure 9 shows that the agreement is remarkable. We also notice that the RDFs of hcp and fcc iron show

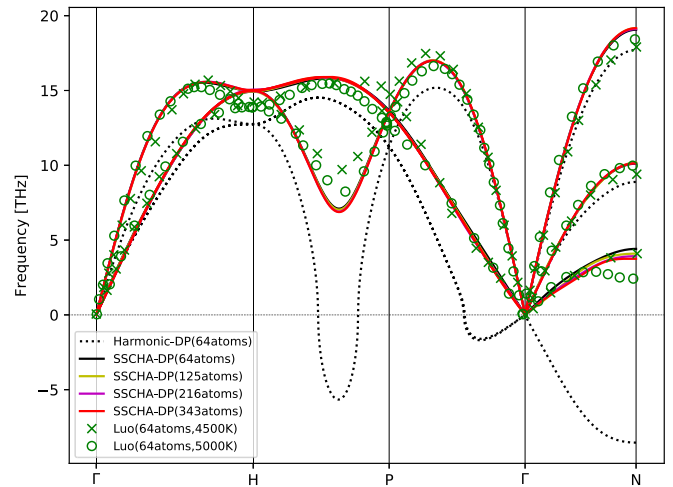


FIG. 8. Phonon spectra of bcc iron at $7.35 \text{ \AA}^3/\text{atom}$ and 5000 K obtained from simulations with the DP model, including anharmonic effects, for different simulation box sizes. The DFT spectrum of Luo *et al.* [13] is also shown for comparison. The phonon instability at 0 K disappears when anharmonic effects are included, in agreement with previous studies.

significant similarity below 4 \AA , with structural differences becoming more pronounced at greater distances. Moreover, distinguishing between the bcc and hcp phases is relatively straightforward based on the features in the RDF at around 3.0 \AA . In this range, a small peak is observed for hcp iron, while for bcc iron, there is a valley. As a result, these solid structures can be distinguished based on their RDF characteristics below 5 \AA , supporting the use of an 8 \AA geometry cutoff for constructing the structural descriptor. It is worth noting that

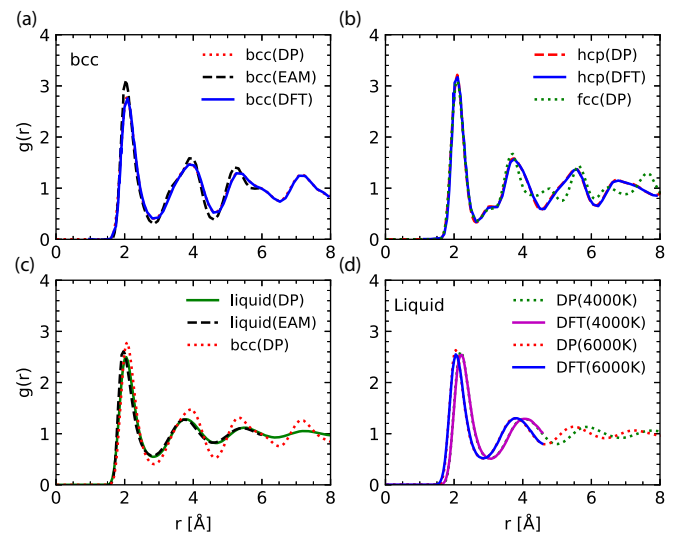


FIG. 9. Radial distribution functions for bcc, fcc, hcp, and liquid iron. Except for (d), all simulations were performed at 360 GPa and 7000 K. (a) RDFs obtained with the EAM [49], DFT, and DP models; (b) RDFs of hcp and fcc iron; (c) RDFs of liquid iron and its comparison with bcc iron. (d) RDFs of the liquid phase at two thermodynamic conditions 4000 K and 9.8 g/cm^3 , and 6000 K and 13.2 g/cm^3 using our DP models compared to DFT data [42].

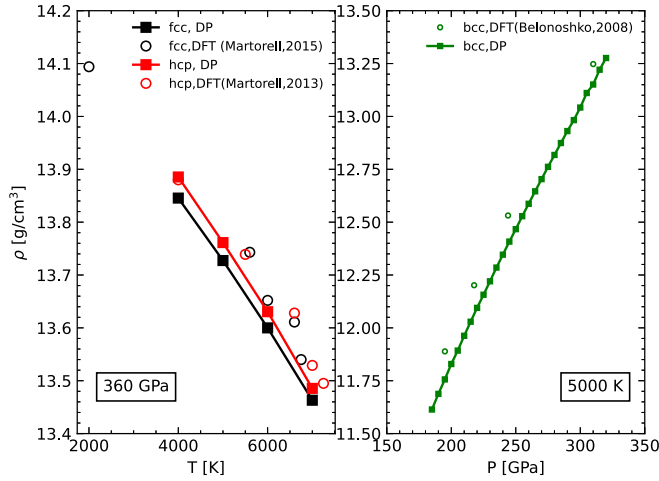


FIG. 10. Pressure-temperature-density relation for bcc, hcp, and fcc iron. For fcc and hcp iron, we performed molecular dynamics simulations in the isobaric-isothermal ensemble using the developed DP models at 360 GPa. These results are compared with previous studies that utilized *ab initio* molecular dynamic simulations [50,51]. For bcc iron, simulations using DP models were executed at a fixed temperature and were compared with the *ab initio* molecular dynamics simulation results by Belonoshko *et al.* [52].

the RDF of bcc iron exhibits a general similarity to the liquid phase. On the other hand, bcc iron displays an asymmetrical shape in its second and third peaks, indicating a long-range structural correlation that differs from that in the liquid phase.

The RDFs of liquid iron from classical molecular dynamics simulations with the EAM potential match well with the DP models, despite the EAM potential having a substantial force error. However, the EAM potential fails to reproduce the DFT and the DP results of the RDF for bcc iron, showing a significant discrepancy in peak intensity. These comparisons highlight the importance of ensuring the microscopic accuracy of the potentials through the force-matching procedure. Similarities in selected physical properties such as RDF, elastic constants, and equation of state may be not sufficient to validate a potential model as they may be due to a cancellation of errors.

G. Equations of state, self-diffusivity, and viscosity for liquid iron at high temperature

Given the small RMSE error in pressure on the testing database, the DP model should provide an accurate description of the equations of state. To demonstrate this, we

conducted molecular dynamics simulations in the isobaric-isothermal ensemble at 360 GPa for fcc and hcp iron, and in the canonical ensemble along the 5000 K isotherm for bcc iron. We then compared the resulting temperature-density and pressure-density relations with those from previous *ab initio* simulations, as illustrated in Fig. 10. As anticipated, a very good agreement was achieved, with discrepancies of less than 1%. The difference is not caused by the inaccuracy of the DP model in reproducing the DFT potential, but rather by differences in the DFT approximations and simulation protocols. As we have seen in Sec. III, the DP model reproduces DFT stresses within $\Delta P = 0.5$ GPa, which corresponds to an error of about 0.05% on the density, if using the P - ρ slope of Fig. 10(b). Indeed, *ab initio* results for hcp and fcc iron exhibit some irregularities, particularly at elevated temperatures, which may originate from the relatively small simulation size and potentially insufficient total simulation time, a problem that does not affect DP simulations.

For liquid iron, pressure values at several temperature-density conditions are shown in Table III, which closely aligns with a prior study [53]. We also computed the self-diffusivity for liquid iron based on the long-time limit of the obtained asymptotic slope of the time-dependent mean-square displacement (MSD). The simulations were conducted on a system with 864 atoms over a duration of 100 ps, and the error bars were calculated from the standard deviation of the results from six independent simulations. The difference compared to previous *ab initio* results is found to be insignificant. Additionally, we determined the viscosity of liquid iron using Kubo-Greenwood relations, with the uncertainty calculated in a similar manner as self-diffusivity. The obtained viscosity remains comparable to previous results. In conclusion, our developed DP models can accurately reproduce not just the thermodynamic properties, but also the dynamical properties observed in DFT results.

IV. GENERALIZED STACKING FAULTS AND VACANCY

All training and validation data sets discussed so far have been obtained from homogeneous bulk phases. However, it is useful to examine the ability of the DP models to reproduce the DFT energy surface in situations that are far from the training data sets, for example in the presence of localized or extended defects. The role of defects is crucial in the understanding of the rheological properties of metals. In the case of solid iron, rheology plays an essential role in determining the thermodynamic evolution of the earth's inner core and the generation of the magnetic field. In this section we examine

TABLE III. Self-diffusivity and viscosity for liquid iron at several thermodynamic conditions calculated using the DP models (DPMD), compared with previous *ab initio* results (AIMD) [53]. The units of density (ρ), temperature (T), pressure (P), viscosity (η), and self-diffusivity (D) are g/cm^3 , K, GPa, mPa s and $10^{-9} \text{m}^2\text{s}^{-1}$, respectively.

ρ	T	AIMD			DPMD		
		P	η	D	P	η	D
10.70	5000	140	6 ± 3	7.0 ± 0.7	136 ± 0.1	6.6 ± 1.3	7.1 ± 0.3
12.13	6000	251	8 ± 3	6 ± 0.6	247.2 ± 0.2	10.0 ± 2.0	6.9 ± 0.2
13.3	6000	360	15 ± 5	5 ± 0.5	351.6 ± 0.1	15.7 ± 2.8	4.9 ± 0.2

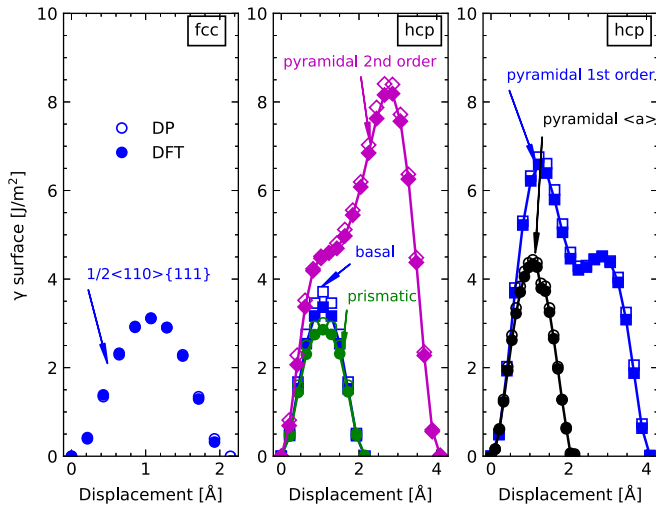


FIG. 11. Prediction of the generalized gamma surface (GSF) energies for several slip systems both fcc and hcp iron, as computed using DP-6000 and DFT models. In all figures, empty symbols represent simulation results from the DP models, whereas solid symbols denote results derived from DFT simulations. For fcc iron, we studied the GSF energies along the $\langle 110 \rangle$ direction on the $\{111\}$ plane. In contrast, for hcp iron, our focus was on multiple slip systems. These include the basal slip ($1/3\langle 2\bar{1}10 \rangle\{0001\}$), prismatic slip ($1/3\langle 2\bar{1}10 \rangle\{01\bar{1}0\}$), pyramidal $\langle a \rangle$ slip ($1/3\langle 2\bar{1}10 \rangle\{01\bar{1}1\}$), pyramidal $\langle c + a \rangle$ first-order slip ($1/3\langle \bar{1}123 \rangle\{01\bar{1}1\}$), and pyramidal $\langle c + a \rangle$ second-order slip ($1/3\langle \bar{1}123 \rangle\{11\bar{2}2\}$).

the DP models' performance in describing the dislocation core properties of solid iron and the formation free energy of a vacancy in hcp iron at inner core pressures.

While the direct simulation of dislocation core structures is feasible for a compact core, dealing with partial dislocations resulting from dissociation proves to be highly computationally expensive in the context of DFT. Considering that many dislocation core structures can be deduced from generalized stacking faults, where the slip between two atomic planes varies from zero to one Burger vector, we place emphasis on calculating these GSF energies using the DP models and then compare with results obtained through DFT simulations. We consider a few common slip systems for both fcc and hcp iron [54], with a simulation cell size of up to 200 atoms. It is important to note that finite-size effects might not be fully accounted for, however, this is beyond the scope of our study. The primary focus of this study is to show the performance of the DP models *vis-a-vis* DFT calculations. As shown in Fig. 11, in all cases, the difference in the calculated energies between DP and DFT remains below 5%. Furthermore, the energy variation as a function of displacement exhibits a remarkably consistent trend. For example, both DP and DFT simulations indicate that the slip along the $\langle \bar{1}123 \rangle$ direction on the $\{11\bar{2}2\}$ plane exhibits a dissociation into two peaks, indicating the presence of partial dislocation. Considering that the GSF configurations were not explicitly part of the training data set, the excellent agreement observed suggests that the DP models are able to describe with excellent accuracy also the local environments encountered by dislocations during their motion.

We compute the formation Gibbs free energy for a vacancy (G_{DP}^f) in hcp iron at 360 GPa and 4000 K using the DP models by

$$G_{\text{DP}}^f = G_{\text{DP}}^{\text{vacancy}} - \frac{n_{\text{perfect}}}{n_{\text{vacancy}}} G_{\text{DP}}^{\text{vacancy}}, \quad (8)$$

where $G_{\text{DP}}^{\text{vacancy}}$ is the Gibbs free energy for hcp iron with a vacancy, G_{DP}^f is the Gibbs free energy for the perfect hcp iron without vacancies. In practice, we employ simulation cells with $n_{\text{perfect}} = 448$ and $n_{\text{vacancy}} = 447$ with a vacancy. The Gibbs free energy was calculated based on the thermodynamic integration method [55]. In this method, the free energy difference between the system of interest and the Einstein crystal is computed. Center-of-mass corrections are introduced following Frenkel and Ladd [55]. The vacancy formation energy in hcp iron at 360 GPa and 4000 calculated with the DP model is $K 8.54 \pm 0.41$ eV. In order to obtain the corresponding DFT value we applied Eq. (7) and found that the difference between G_{DP}^f and G_{DFT}^f is 0.64 eV. While this value may seem large compared to the accuracy reached by the DP in the ideal bulk systems, it must be considered that accuracies for bulk systems refer to energy values per atom, while the formation energy of a single vacancy is obtained the total energy of simulations with several hundred atoms and in the presence of large thermal disorder.

V. CONCLUSIONS

In this study, we have developed a set of deep-potential interatomic models for hcp, bcc, fcc, and liquid iron that cover a wide range of conditions of relevance for the earth's core, spanning pressures from 75–650 GPa and temperatures from 4000–7600 K. These models achieve *ab initio* accuracy while maintaining computational efficiency, thereby enabling large-scale simulations.

To account for temperature-dependent thermal electronic excitations, we generated distinct potentials for various temperatures, specifically at 4000, 5000, 6000, 7000, and 7600 K. To evaluate the performance of our developed DP models, we established an independent testing data set and found that their performance on the testing data set closely mirrored that on the training data set, indicating that our DP models neither suffer from underfitting nor overfitting issues. Moreover, the performance remains consistent across varying temperatures and pressures. We further assessed their performance in larger systems, containing over 1000 atoms, confirming the suitability of the DP models for large-scale simulations.

As one of our objectives is to determine the thermodynamic stability of the solid phases, it is crucial to understand the accuracy of the Gibbs free energy in these DP models. To achieve this, we applied the free energy perturbation theory to estimate the Gibbs free energy difference between the DP models and DFT, and found it to be consistently less than 6 meV/atom. Remarkably, this difference is shown to be independent of pressure, temperature, and the number of atoms, further confirming the applicability of these models to large-scale simulations. We also compared physical properties, such as the phonon spectra, equations of state, and radial distribution functions,

calculated using the DP models against *ab initio* results, and found that the agreement is excellent.

Collectively, these validations highlight the DP models' ability to accurately replicate all thermodynamic and dynamical properties present in the training data sets. To explore the extent to which the DP models can describe physical properties that depend on microscopic configurations that are not explicitly included in the training data sets, we considered generalized stacking fault energies. The remarkable agreement obtained also in this case suggests that the DP models are able to describe the local environments encountered by dislocations during their motion. Consequently, we believe that the developed DP models have a wide range of potential

applications and will play a pivotal role in elucidating the thermodynamic and rheological properties of iron at extreme conditions [56].

ACKNOWLEDGMENTS

We acknowledge the CINECA (Consorzio Interuniversitario per il Calcolo Automatico) award, under the IS CRA initiative and Leonardo early access program, for the availability of high-performance computing resources and support. L.Z. also thanks Victor Robinson and Rongrong Xie for useful discussions on the construction of deep-learning interatomic potentials.

-
- [1] K. Hirose, S. Labrosse, and J. Hernlund, Composition and state of the core, *Annu. Rev. Earth Planet Sci.* **41**, 657 (2013).
- [2] A. Laio, S. Bernard, G. Chiarotti, S. Scandolo, and E. Tosatti, Physics of iron at earth's core conditions, *Science* **287**, 1027 (2000).
- [3] D. Alfe, M. Gillan, and G. Price, The melting curve of iron at the pressures of the earth's core from *ab initio* calculations, *Nature (London)* **401**, 462 (1999).
- [4] L. Vočadlo, D. Alfè, M. Gillan, I. Wood, J. Brodholt, and G. D. Price, Possible thermal and chemical stabilization of body-centred-cubic iron in the earth's core, *Nature (London)* **424**, 536 (2003).
- [5] A. B. Belonoshko, R. Ahuja, and B. Johansson, Stability of the body-centred-cubic phase of iron in the earth's inner core, *Nature (London)* **424**, 1032 (2003).
- [6] A. B. Belonoshko, N. V. Skorodumova, S. Davis, A. N. Osipov, A. Rosengren, and B. Johansson, Origin of the low rigidity of the earth's inner core, *Science* **316**, 1603 (2007).
- [7] A. B. Belonoshko, N. V. Skorodumova, A. Rosengren, and B. Johansson, Elastic anisotropy of earth's inner core, *Science* **319**, 797 (2008).
- [8] S. Tateno, K. Hirose, Y. Ohishi, and Y. Tatsumi, The structure of iron in earth's inner core, *Science* **330**, 359 (2010).
- [9] R. G. Kraus, R. J. Hemley, S. J. Ali, J. L. Belof, L. X. Benedict, J. Bernier, D. Braun, R. Cohen, G. W. Collins, F. Coppari *et al.*, Measuring the melting curve of iron at super-earth core conditions, *Science* **375**, 202 (2022).
- [10] S. Anzellini, A. Dewaele, M. Mezouar, P. Loubeyre, and G. Morard, Melting of iron at earth's inner core boundary based on fast x-ray diffraction, *Science* **340**, 464 (2013).
- [11] R. Sinmyo, K. Hirose, and Y. Ohishi, Melting curve of iron to 290 GPa determined in a resistance-heated diamond-anvil cell, *Earth Planet. Sci. Lett.* **510**, 45 (2019).
- [12] A. B. Belonoshko, T. Lukinov, J. Fu, J. Zhao, S. Davis, and S. I. Simak, Stabilization of body-centred cubic iron under inner-core conditions, *Nature Geoscience* **10**, 312 (2017).
- [13] W. Luo, B. Johansson, O. Eriksson, S. Arapan, P. Souvatzis, M. I. Katsnelson, and R. Ahuja, Dynamical stability of body center cubic iron at the earth's core conditions, *Proc. Natl. Acad. Sci. (USA)* **107**, 9962 (2010).
- [14] B. Godwal, F. González-Cataldo, A. Verma, L. Stixrude, and R. Jeanloz, Stability of iron crystal structures at 0.3–1.5 TPa, *Earth Planet. Sci. Lett.* **409**, 299 (2015).
- [15] M. Mattesini, A. B. Belonoshko, E. Bufo, M. Ramírez, S. I. Simak, A. Udías, H.-K. Mao, and R. Ahuja, Hemispherical anisotropic patterns of the earth's inner core, *Proc. Natl. Acad. Sci. (USA)* **107**, 9507 (2010).
- [16] S. Ritterbex and T. Tsuchiya, Viscosity of hcp iron at earth's inner core conditions from density functional theory, *Sci. Rep.* **10**, 6311 (2020).
- [17] A. B. Belonoshko, J. Fu, and G. Smirnov, Free energies of iron phases at high pressure and temperature: Molecular dynamics study, *Phys. Rev. B* **104**, 104103 (2021).
- [18] W. Kohn and L. J. Sham, Self-consistent equations including exchange and correlation effects, *Phys. Rev.* **140**, A1133 (1965).
- [19] P. Hohenberg and W. Kohn, Inhomogeneous electron gas, *Phys. Rev.* **136**, B864 (1964).
- [20] N. D. Mermin, Thermal properties of the inhomogeneous electron gas, *Phys. Rev.* **137**, A1441 (1965).
- [21] J.-P. Poirier, *Introduction to the Physics of the Earth's Interior* (Cambridge University Press, Cambridge, 2000).
- [22] V. Bulatov and W. Cai, *Computer Simulations of Dislocations* (Oxford University Press, Oxford 2006), Vol. 3.
- [23] D. Alfè, G. D. Price, and M. J. Gillan, Iron under earth's core conditions: Liquid-state thermodynamics and high-pressure melting curve from *ab initio* calculations, *Phys. Rev. B* **65**, 165118 (2002).
- [24] A. S. Mikhaylushkin, S. I. Simak, L. Dubrovinsky, N. Dubrovinskaia, B. Johansson, and I. A. Abrikosov, Pure iron compressed and heated to extreme conditions, *Phys. Rev. Lett.* **99**, 165505 (2007).
- [25] A. P. Bartók, M. C. Payne, R. Kondor, and G. Csányi, Gaussian approximation potentials: The accuracy of quantum mechanics, without the electrons, *Phys. Rev. Lett.* **104**, 136403 (2010).
- [26] L. Zhang, J. Han, H. Wang, R. Car, and Weinan E, Deep potential molecular dynamics: A scalable model with the accuracy of quantum mechanics, *Phys. Rev. Lett.* **120**, 143001 (2018).
- [27] L. Zhang, H. Wang, R. Car, and E. Weinan, Phase diagram of a deep potential water model, *Phys. Rev. Lett.* **126**, 236001 (2021).
- [28] E. Sola and D. Alfe, Melting of iron under earth's core conditions from diffusion Monte Carlo free energy calculations, *Phys. Rev. Lett.* **103**, 078501 (2009).
- [29] A. Dewaele, B. Amadon, A. Bosak, V. Svitlyk, and F. Occelli, Synthesis of single crystals of ϵ -iron and direct

- measurements of its elastic constants, *Phys. Rev. Lett.* **131**, 034101 (2023).
- [30] A. Dewaele, P. Loubeyre, F. Occelli, M. Mezouar, P. I. Dorogokupets, and M. Torrent, Quasihydrostatic equation of state of iron above 2 Mbar, *Phys. Rev. Lett.* **97**, 215504 (2006).
- [31] D. Alfè, G. D. Price, and M. J. Gillan, Thermodynamics of hexagonal-close-packed iron under earth's core conditions, *Phys. Rev. B* **64**, 045123 (2001).
- [32] P. Giannozzi, S. Baroni, N. Bonini, M. Calandra, R. Car, C. Cavazzoni, D. Ceresoli, G. L. Chiarotti, M. Cococcioni, I. Dabo *et al.*, QUANTUM ESPRESSO: A modular and open-source software project for quantum simulations of materials, *J. Phys.: Condens. Matter* **21**, 395502 (2009).
- [33] P. Giannozzi, O. Andreussi, T. Brumme, O. Bunau, M. B. Nardelli, M. Calandra, R. Car, C. Cavazzoni, D. Ceresoli, M. Cococcioni *et al.*, Advanced capabilities for materials modelling with QUANTUM ESPRESSO, *J. Phys.: Condens. Matter* **29**, 465901 (2017).
- [34] P. E. Blöchl, Projector augmented-wave method, *Phys. Rev. B* **50**, 17953 (1994).
- [35] J. P. Perdew, K. Burke, and M. Ernzerhof, Generalized gradient approximation made simple, *Phys. Rev. Lett.* **77**, 3865 (1996).
- [36] H. J. Monkhorst and J. D. Pack, Special points for Brillouin-zone integrations, *Phys. Rev. B* **13**, 5188 (1976).
- [37] P. Hirel, Atomsk: A tool for manipulating and converting atomic data files, *Comput. Phys. Commun.* **197**, 212 (2015).
- [38] Y. Zhang, C. Gao, Q. Liu, L. Zhang, H. Wang, and M. Chen, Warm dense matter simulation via electron temperature dependent deep potential molecular dynamics, *Phys. Plasmas* **27**, 122704 (2020).
- [39] G. Ackland, Temperature dependence in interatomic potentials and an improved potential for Ti, *J. Phys.: Conf. Ser.* **402**, 012001 (2012).
- [40] H. Wang, L. Zhang, J. Han, and E. Weinan, DeePMD-kit: A deep learning package for many-body potential energy representation and molecular dynamics, *Comput. Phys. Commun.* **228**, 178 (2018).
- [41] L. Zhang, J. Han, H. Wang, W. Saidi, R. Car, and W. E, End-to-end symmetry preserving inter-atomic potential energy model for finite and extended systems, in *Advances in Neural Information Processing Systems*, edited by S. Bengio, H. Wallach, H. Larochelle, K. Grauman, N. Cesa-Bianchi, and R. Garnett (Curran Associates, Red Hook, 2018), Vol. 31.
- [42] Z. Li, R. Caracas, and F. Soubiran, Partial core vaporization during giant impacts inferred from the entropy and the critical point of iron, *Earth Planet. Sci. Lett.* **547**, 116463 (2020).
- [43] S. Plimpton, Fast parallel algorithms for short-range molecular dynamics, *J. Comput. Phys.* **117**, 1 (1995).
- [44] D. J. Evans and B. L. Holian, The Nose–Hoover thermostat, *J. Chem. Phys.* **83**, 4069 (1985).
- [45] M. Parrinello and A. Rahman, Polymorphic transitions in single crystals: A new molecular dynamics method, *J. Appl. Phys.* **52**, 7182 (1981).
- [46] C. Chipot and A. Pohorille, Calculating free energy differences using perturbation theory, in *Free Energy Calculations: Theory and Applications in Chemistry and Biology* (Springer, Berlin, 2007), pp. 33–75.
- [47] C. Vega, E. Sanz, J. Abascal, and E. Noya, Determination of phase diagrams via computer simulation: Methodology and applications to water, electrolytes and proteins, *J. Phys.: Condens. Matter* **20**, 153101 (2008).
- [48] L. Monacelli, R. Bianco, M. Cherubini, M. Calandra, I. Errea, and F. Mauri, The stochastic self-consistent harmonic approximation: Calculating vibrational properties of materials with full quantum and anharmonic effects, *J. Phys.: Condens. Matter* **33**, 363001 (2021).
- [49] A. B. Belonoshko, J. Fu, T. Bryk, S. I. Simak, and M. Mattesini, Low viscosity of the earth's inner core, *Nature Commun.* **10**, 2483 (2019).
- [50] B. Martorell, L. Vočadlo, J. Brodholt, and I. G. Wood, Strong premelting effect in the elastic properties of hcp-fe under inner-core conditions, *Science* **342**, 466 (2013).
- [51] B. Martorell, J. Brodholt, I. G. Wood, and L. Vočadlo, The elastic properties and stability of fcc-Fe and fcc-FeNi alloys at inner-core conditions, *Geophys. J. Int.* **202**, 94 (2015).
- [52] A. B. Belonoshko, P. I. Dorogokupets, B. Johansson, S. K. Saxena, and L. Koči, *Ab initio* equation of state for the body-centered-cubic phase of iron at high pressure and temperature, *Phys. Rev. B* **78**, 104107 (2008).
- [53] D. Alfè, G. Kresse, and M. J. Gillan, Structure and dynamics of liquid iron under earth's core conditions, *Phys. Rev. B* **61**, 132 (2000).
- [54] P. Tu, Y. Zheng, C. Zhuang, X. Zeng, and H. Zhu, A high-throughput computation framework for generalized stacking fault energies of pure metals, *Comput. Mater. Sci.* **159**, 357 (2019).
- [55] D. Frenkel and A. J. Ladd, New Monte Carlo method to compute the free energy of arbitrary solids. Application to the fcc and hcp phases of hard spheres, *J. Chem. Phys.* **81**, 3188 (1984).
- [56] Z. Li and S. Scandolo (unpublished).